

Decoding Atomic-Level Structures of the Interface between Pt Subnanocrystals and Nanostructured Carbon

Hongye Cheng,[†] Ingvar Kvande,[‡] Yi-An Zhu,^{,†} Nina Hammer,[‡] Magnus Rønning,[‡]*

John C. Walmsley,[§] Ping Li,[†] Zhiwen Qi,[†] Xing-Gui Zhou,[†] De Chen^{,‡}*

[†]UNILAB, State Key Laboratory of Chemical Engineering, Shanghai Key Laboratory of
Multiphase Materials Chemical Engineering, East China University of Science and Technology,
Shanghai 200237, China

[‡]Department of Chemical Engineering, Norwegian University of Science and Technology, N-
7491 Trondheim, Norway

[§]SINTEF Materials and Chemistry, N-7491 Trondheim, Norway

*Corresponding author: yanzhu@ecust.edu.cn (Yi-An Zhu), chen@nt.ntnu.no (De Chen).

ABSTRACT

Gaining an insight into the interface structure resulting from the interaction between metal nanoparticles and their supports, particularly under relevant reaction conditions, has been an important topic in heterogeneous catalysis and materials science. In this contribution, the active sites and interfaces of Pt subnanocrystals supported on carbon nanofibers (CNFs) are investigated and visualized at the atomic level by highly integrated XANES, EXAFS, and molecular dynamics (MD) simulations based on a reactive force field. Experimental and theoretical results indicate that the surface structure of the CNFs is one of the key parameters that govern the metal-support interface structure, which in turn determines the metal-support interaction strength and the structural properties of Pt clusters, including cluster size, Pt coordination number, and Pt-Pt bond length. Owing to the strong interaction between Pt and CNFs, sub-nanometer-sized Pt clusters are stabilized on CNFs. The Pt-Pt coordination number determined from EXAFS suggests Pt clusters of ~ 1 nm in size are deposited on platelet-type CNFs (p-CNFs) while clusters smaller than 0.6 nm are supported on fishbone-type CNFs (f-CNFs). The catalysts exhibit high selectivity toward CO oxidation at relatively low temperatures in the presence of H_2 , and their activity is related to the Pt coordination number and Pt-Pt bond length. The Pt clusters on the p-CNFs with relatively high coordination number has much higher activity than those on f-CNFs. The combined EXAFS analysis and MD simulations provide a better understanding of the catalyst properties at the atomic level and pave the way to use the CNF structure as a platform to tune the Pt particle size and metal activity through manipulating the metal-support interaction.

KEYWORDS

EXAFS; XANES; Molecular Dynamics Simulation; Preferential CO Oxidation

1. Introduction

Metal-support interaction has long been recognized as a vital factor in determining metal reactivity in heterogeneous catalysis. However, control of the metal-support interaction has only achieved limited success due to the complexity in its physical nature. Thanks to the progress in controllable synthesis of carbon nanofibers (CNFs) and their tunable surface structures with different graphene sheet orientations with respect to the principal axis,¹ CNFs have been used as a platform to tune the metal reactivity through manipulating the metal-support interaction.²⁻⁵ It has been reported that the surface structures of CNFs can significantly influence the activity and selectivity of supported Pt nanoparticles in proton exchange membrane (PEM) fuel cells,⁶ dehydrogenation,⁷ and hydrogen oxidation reactions.⁸ For instance, traces of CO in H₂ are known to poison the anode reaction in fuel cells and, consequently, preferential oxidation of CO in H₂-rich stream is of crucial importance for fuel cell catalysts. In this regard, the orientation of graphene sheets and the presence of oxygenated groups on the CNF surfaces prove to have a significant effect on the adsorption behavior of CO (and hence the CO oxidation activity) on the Pt nanoparticles.⁸ Therefore, a better understanding of the microstructures of the metal-CNF interfaces is essential to the improvement of our ability to tailor the metal-support interaction to better catalyst activity, selectivity, and stability. It relies not only on advanced synthesis of the CNF-supported catalysts with well-controlled support structures and well-defined metal particle sizes and shapes, but also on detailed characterization of the interface.

Most of the CNF-supported catalysts are characterized by temperature-programmed oxidation (TPO), chemisorption measurements, and transmission electron microscopy (TEM). Due to the limitation in resolution in particular images, the determination of metal particle size smaller than 2 nm from TEM results is a challenge.⁹ On the other hand, extended X-ray absorption fine

structure (EXAFS) is a method that gives element-specific information about the local environment, which can provide new insight into the metal-CNF interface and accurately determine the particle size of sub-nanometer Pt clusters from the derived coordination number. So far, however, only a few such studies have been reported. For $[\text{Pd}(\text{NH}_3)_4]^{2+}$ deposited on CNF by ion-exchange, EXAFS analysis revealed a significant metal-CNF interaction both before and after reduction, where the Pd complex was found to be stabilized by the carboxylic groups on the surface as well as the π -system of the support.¹⁰ In another study, EXAFS results of CNF-supported Pt catalysts prepared by deposition-precipitation indicated that each interfacial Pt atom has four carbon neighbors and is bonded to two adjacent layers of armchair or zigzag arrangements.¹¹ By contrast, each Pt atom at the Pt-Vulcan carbon interface was found to have six carbon neighbors, which was explained by the adsorption of Pt on a basal plane site.¹¹ Despite these studies, knowledge and understanding of the fine structures of the metal-CNF interface and how the interface structure could affect the geometrical and electronic structures of supported metal particles is still very limited. It has been suggested that successful solutions to these nanostructure problems will involve a “complex modeling” paradigm that combines theory and experiment in a self-consistent computational framework.¹²

Molecular dynamics (MD) simulation based on reactive force fields proves to be a powerful technique that is capable of providing detailed insight into the interaction between metal nanoparticles and supports at an atomic level. Sanz-Navarro et al. deposited Pt and Ni nanoparticles of about 100 atoms on the edge and basal planes of both p-CNFs and f-CNFs, exploring the metal-support interactions by MD simulations based on a bond-order force field.¹³⁻

¹⁵ Because of the strong interaction between the Pt nanoparticles and CNFs, the Pt-Pt bonds on the supported Pt nanoparticles are elongated and a significant cluster reconstruction was

observed. More recently, MD simulations were carried out using the same force fields to examine the effect of the variable morphologies of f-CNFs on the microstructure of supported Pt₁₀₀ clusters.¹⁶ The cone-helix f-CNF models with different basal-to-edge surface area ratios and edge plane terminations were constructed. It was found that the Pt atoms at the Pt-CNF interface prefer to be bonded to basal planes as the apex angle is decreased or hydrogen termination is introduced. Simultaneously, both the binding energies of the Pt₁₀₀ clusters to the f-CNFs and the degree of Pt cluster reconstruction are lowered. In contrast, if more CNF edge planes are exposed, a higher Pt dispersion, lower first-shell Pt-Pt coordination numbers, and longer Pt-Pt surface bonds are attained, which arise from a stronger Pt-CNF interaction.

Given the atomic-level structural information provided by EXAFS analysis and MD simulation, the interplay between these two techniques makes it possible to reproduce the interface structure of the supported metal catalysts and can indeed guide the development of new catalysts with improved catalytic properties. In this contribution, X-ray Absorption Near Edge Structure (XANES) experiment is first carried out to measure the interaction between Pt particles and CNF supports. Next, EXAFS analysis is performed to elucidate the fine structures of Pt sub-nanoparticles and Pt-CNF interfaces. After that, on the basis of the EXAFS results such as coordination numbers and bond lengths of Pt-Pt and Pt-C bonds, CNF-supported Pt sub-nanoparticles are constructed and relaxed at the atomic level by MD simulations employing the ReaxFF force field. Finally, in order to unravel the observed significant effects of the CNF surface structure on the catalytic properties of the catalysts, the reactivity of the CNF-supported Pt catalysts and the catalytic consequence of the Pt-CNF interaction are investigated in preferential oxidation of CO by integrating the results from kinetic study, EXAFS analysis, and MD simulation.

2. Experimental and Computational Details

2.1. Experimental

CNFs were grown by catalytic chemical vapor deposition.¹⁷⁻¹⁹ The p-CNFs were synthesized from Fe nanoparticles in a mixture of CO and H₂, followed by purification in 4M HCl at 50°C for 4 times and each time for 2 hours.²⁰ The f-CNFs were grown using CO and a Ni/SiO₂ catalyst and was purified in NaOH.²⁰ No Ni and Fe content were detected by X-ray photoelectron spectroscopy (XPS) and TEM on the surfaces of the CNFs.^{8, 20}

Due to improved control of the formation and deposition of Pt, the majority of recent work concerning the preparation of CNF- or carbon nanotube (CNT)-supported Pt catalysts has employed colloidal methods. In particular, a metal-oxide colloid method has been developed by Reetz and co-workers,²¹⁻²² which was adopted in this work to prepare the supported Pt catalysts under basic conditions (at pH values of 9-10), using H₂PtCl₆ as a precursor and Li₂CO₃ as a base.^{17, 21-22}

X-ray adsorption spectrum (XAS) data were collected using the facilities of the Swiss-Norwegian Beamlines (SNBL) at the European Synchrotron Radiation Facility (ESRF), France. Spectra were collected at the Pt-L₃ edge. The data were collected in the fluorescence mode and a Lytle type water-cooled furnace was used for the in-situ treatment of the samples. The XAS data analysis program WinXAS (version 3.1)²³ was used for background subtraction and normalisation of the spectra. Model fitting was carried out with *EXCURV98* using curved-wave theory and *ab initio* phase shifts.²⁴⁻²⁵ The EXAFS spectra were least-squares fitted in *k* space using *k*³ weighted data. A Pt metal foil and PtO₂ were used as model compounds to check the validity of the *ab initio* phase shifts and to establish the amplitude reduction factor (AFAC).

Transmission electron microscopy (TEM) and scanning transmission electron microscopy (STEM) in high angle annular dark field (HAADF) mode were used to study the morphologies and size distributions of the Pt clusters. The investigation was carried out on a JEOL 2010F electron microscope with an acceleration voltage of 200 kV. The electrochemical (active) surface area (ESA) was determined from the underpotential deposition charge of hydrogen from CV measurements. A catalytic ink was prepared by suspending 2-3 mg catalyst in 2 mL isopropanol. A diluted Nafion solution was added to the ink so that the amount of Nafion was 5 wt% with respect to the catalyst. The titanium plate was polished and etched carefully in 10 % HCl to remove the oxide layer. The catalyst slurry was ultrasonicated for 15 minutes following a spray to the polished titanium plate. The clean plate was placed on a hotplate fixed at 80°C, and the slurry was sprayed on using an airbrush. The amount of catalyst on the electrode was found by weighing the plate before and after spraying. CV measurements were recorded at 200 mV/s and 100 mV/s using a Zahner IM6e potentiostat in a three electrode setup; reference electrode was a Redrod electrode (Radiometer), and a Pt foil acted as counter electrode. The electrolyte was 0.5 M H₂SO₄. After subtraction of the double layer charge, the EAS of the catalysts was calculated by assuming that a smooth Pt electrode gives a hydrogen adsorption charge of 210 $\mu\text{C}/\text{cm}^2$.²⁶ To investigate the difference between pre-reduced and as-prepared catalysts, portions of the catalysts were transferred to a quartz cup and placed in a tubular furnace. The samples were treated in an atmosphere containing 7 % H₂ in Ar, heated from room temperature to 175°C at a rate of 5°C/min. The temperature was held at 175°C for 30 minutes, before the gas supply was changed to Ar and the sample was allowed to cool down.

The activity tests were conducted in a quartz U-tube fixed-bed reactor with an inner diameter of 3.5 mm under conditions identical to previous work.⁸ A catalyst amount corresponding to 0.08

mg Pt were mixed with 100 mg SiC-particles (45 mm) as diluent to minimize the temperature gradient in the reactor. The catalysts were reduced in a 5 % H₂/He mixture at 175°C (5°C/min) for 30 min. The temperature-programmed surface reaction was then performed from 25°C to 200°C with a heating rate of 1°C/min procedure in a H₂/O₂/He mixture with and without CO, containing H₂ (8 ml/min), and O₂ (4 ml/min) diluted with He (800 ml/min). The low pressure of reactants, high flow rate and large amount of diluents were used to keep reaction isothermal. For the preferential CO oxidation experiments, a gas containing 1 mole% of CO/H₂ stored in a steel-coated bottle was used. The conversion was calculated based on the O₂-concentration obtained by an online micro-GC (Agilent 3000).

2.2. Computational

MD simulations have been performed by using the LAMMPS code²⁷⁻²⁸ and the ReaxFF reactive force field. The ReaxFF is based on a bond-order approach and a charge equilibrium scheme,²⁹ which proved successful in our previous work in representing formation and breaking Pt-C, Pt-Pt, and C-C bonds.^{14-16, 30} A time step of 0.25 fs was employed. It took 50 ps to equilibrate the systems at 600 K using the canonical ensemble (NVT) and Nosé-Hoover chain thermostat.³¹ MD simulations were then carried out in equilibrium for 150 ps.

In order to make a direct comparison between experimental observations and simulated results, Pt₁₃ and Pt₅₀ clusters which have particle sizes of about 0.56 nm and 1.14 nm, respectively, were constructed on the basis of the face-centered cubic (FCC) Pt crystal structure. Pt₅₀ clusters were supported on armchair and zigzag arrangements of the p-CNF, while Pt₁₃ clusters were supported on the surfaces of the f-CNF. Simulated annealing was performed to get stable clusters before the Pt clusters were deposited.

The p-CNFs with armchair and zigzag arrangements exposed were represented as 18 layers of graphite with dimensions of $5.965 \text{ nm} \times 6.030 \text{ nm} \times 2.952 \text{ nm}$ and $5.903 \text{ nm} \times 6.030 \text{ nm} \times 2.983 \text{ nm}$, respectively, and the neighboring graphite slabs were separated from each other by a vacuum region of around 6 nm in the direction parallel to the graphite basal planes, as shown in Figure 1a and 1b. During the MD simulations, the C atoms in the bottom half slab were fixed at their crystallographic positions. The cone-helix f-CNF model with a disclination angle of 240° was employed in the present work, which was obtained with a continuous graphite ribbon spiraling along the principal axis.¹ The resultant f-CNF model has an apex angle of 38.97° , which is close to that of the f-CNF prepared in experiment ($\sim 42^\circ$). Four helical cones with outer diameter of 6 nm are included in a unit cell with dimensions of $15 \text{ nm} \times 15 \text{ nm} \times 4.067 \text{ nm}$, as shown in Figure 1c and 1d.

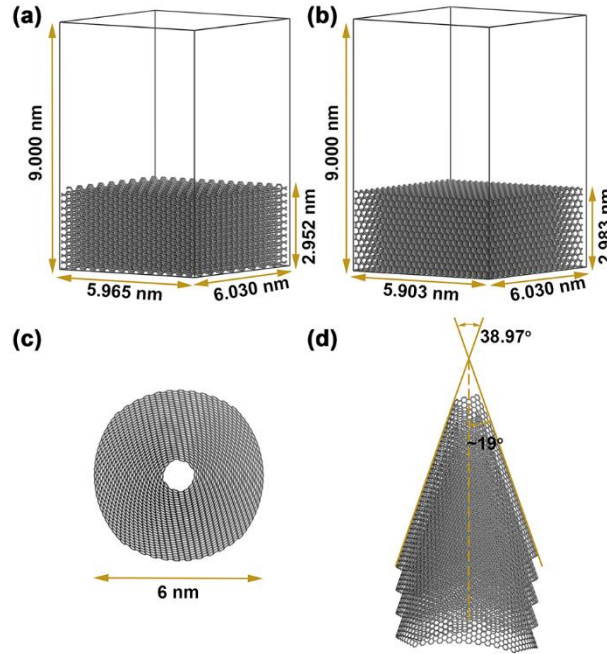


Figure 1. Schematic representations of the p-CNF models with (a) armchair and (b) zigzag arrangements exposed and (c) top and (d) side views of the f-CNF models.

3. Results and Discussion

3.1. Properties of Pt nanoparticles supported on CNFs

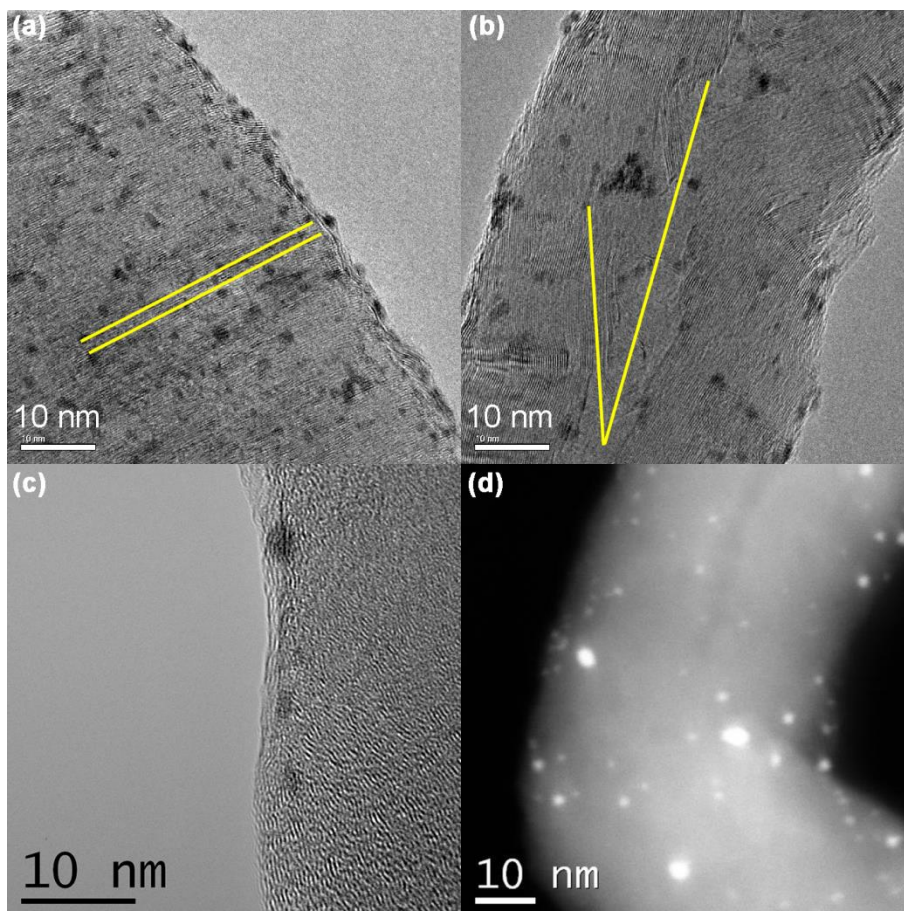


Figure 2. TEM images of Pt/p-CNFs (a) and Pt/f-CNFs (b and c), and HAADF-STEM image of Pt/f-CNFs (d).

The structures of the CNFs used in this work are identical to the ones used in our previous study where the effects of the properties of carbon supports on the dispersion of Pt-oxide colloids were investigated.²⁰ Some characterization data from the previous study are summarized here. The p-CNFs have a BET surface area of 144 m²/g while the f-CNFs have a surface area of 93 m²/g. The p-CNFs (Figure 2a) have graphite layers stacked perpendicularly with respect to the fiber axis.

Meanwhile, the f-CNFs (Figure 2b) have an average stacking angle (half of apex angle) of 20-25°. The interplanar spacing of the p-CNFs (0.336 nm) is close to that of graphite while the value is significantly larger (0.344 nm) in the f-CNFs. The difference in interplanar spacing between the p-CNFs and f-CNFs can be explained by the greater lattice strain at smaller CNF apex angles.¹ Apart from open edges, closed layers and irregular structures can also be found on the surfaces of both CNFs. From XPS, the p-CNFs were found to have far more structures corresponding to sp³-hybridized and/or disordered carbon and/or dangling bonds.²⁰

Table 1. The loading, surface area, and particle size of Pt nanoparticles supported on p-CNFs and f-CNFs

Sample name	Preparation Method	Loading ^a [wt %]	CV ^b		TEM ^c
			Surface area [m ² /g]	Particle size [nm]	Particle size [nm]
Pt/p-CNF	metal-oxide colloid	3.5	129	2.3	1.7
Pt/f-CNF	metal-oxide colloid	3.0	176	1.9	1.8

^a Obtained from TPO

^b Pre-reduced

^c As-prepared

The Pt particle sizes given in Table 1 were estimated by statistical analysis of particles from HRTEM images and hydrogen adsorption measured by CV. The size of the metal-oxide colloids prepared by the same method was reported to be in the range 1-2 nm elsewhere.²¹ TEM suggests an almost identical Pt particle size for the Pt/p-CNFs and Pt/f-CNFs (1.7 - 1.8 nm). However, CV measurements indicate that the Pt surface area of the Pt/f-CNFs is significantly higher than that of the Pt/p-CNFs. It corresponds to the particle size of 2.3 nm and 1.9 nm for the pre-reduced Pt nanoparticles on the Pt/p-CNFs and Pt/f-CNFs, respectively. The discrepancy between the results

obtained from the two techniques indicate that accurate determination of the size of nanoparticles is quite challenging. Indeed, TEM has a limited ability to characterize the sub-nanometer metal particles, and CV measurements usually overestimate the nanoparticle size because it is difficult to achieve a full monolayer adsorption of atomic hydrogen under experimental conditions and the impurities in electrolytes may sometimes be strongly adsorbed on the metal particles.³²

3.2. Pt-CNF interaction

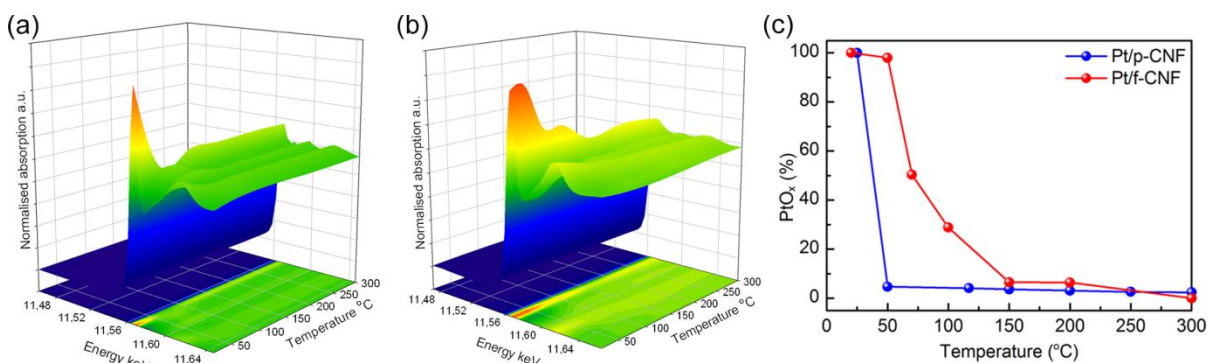


Figure 3. 3D contour plots of XANES data during reduction in 5 % H₂/He on the (a) Pt/p-CNFs and (b) Pt/f-CNFs and (c) fraction of PtO_x (%) obtained from XANES analysis.

The interaction of the Pt clusters with the CNFs was studied by temperature-programmed reduction (TPR) in conjunction with XANES.³³ The fraction of PtO_x and Pt were estimated based on the XANES data as a function of reduction temperature during the TPR experiment (see Figure 3a and 3b). The changes in the PtO_x fraction as a function of reduction temperature are shown in Figure 3c. An immediate onset of reduction of PtO_x was observed at room temperature for the Pt/p-CNFs and the reduction is nearly accomplished at 50°C. Even temperature is increased to 300°C, a fraction of PtO_x (2.4 wt%) still persists in the sample. Although the detected Pt²⁺ fraction upon reduction is small, the possibility of the presence of oxygen between Pt and C and/or positively charged Pt **due to electron transfer between the Pt**

and p-CNFs cannot be disregarded. By contrast, the Pt/f-CNFs are reduced at a higher temperature and in two steps. The majority of the Pt (90 %) is reduced at 150°C while the reduction of a minor fraction is completed up to 300°C. It can therefore be deduced that the interaction between the Pt clusters with the f-CNFs is much stronger than that with the p-CNFs.

3.3. Fine structures of supported Pt nanoparticles

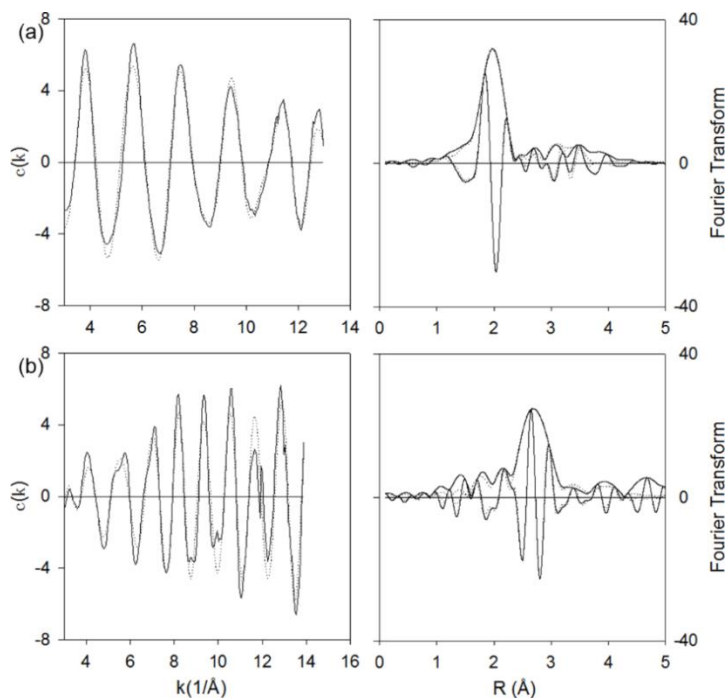


Figure 4. Pt L_{III} EXAFS spectra (left) and the corresponding Fourier transform (right) of Pt/p-CNFs (a) as-prepared and (b) after 1 hour of reduction at 300°C. Experimental data are shown in solid lines and the k^3 fit in dotted lines.

EXAFS is a technique of extraordinary power to represent the fine structures of metal particles and metal-support interfaces. Experimental and fitted EXAFS data of the as-prepared and reduced Pt/p-CNFs are presented in Figure 4. The results from EXAFS analysis, including Pt-O and Pt-Pt coordination numbers as well as interatomic distances, are summarized in Table 2.

From the table, it can be seen that the EXAFS analysis of the as-prepared PtO/p-CNFs shows similar first-shell Pt-O coordination number and Pt-O bond length to those in the PtO₂. This finding suggests that the platinum oxide nanoparticles maintain their crystal structure upon deposition on CNFs and that the auto-reductive effect of the carbon supports is not able to reduce the oxide particles. In addition, there are only minor contributions from the more distant Pt-Pt shell to the EXAFS signal of the Pt oxide nanoparticles, indicating that the particles are relatively small. In a previous study, the presence of hydroxyl-metal moieties has been suggested for particles deposited through the metal-oxide colloid method.³⁴ The small particle size makes it difficult to infer from the EXAFS data whether the particles are present as hydroxides or oxides before reduction, because the first-shell parameters are quite close for the two cases.

Table 2. Coordination number and interatomic distances determined from EXAFS analysis

Sample	Scatter	Coordination Number	Interatomic distance [nm]	$2s^2$ [\AA^2] ^a
PtO ₂	Pt-O	6	0.203	0.007
	Pt-Pt	12	0.311	0.011
Pt-O/p-CNF	Pt-O	5.3	0.201	0.007
	Pt-Pt	1.5	0.306	0.009
Pt foil	first Pt-Pt shell	12	0.278	0.010
	second Pt-Pt shell	6	0.393	0.016

^a Debye-Waller type factor

From the EXAFS data given in Table 3, the first-shell Pt-Pt coordination number in the reduced Pt/p-CNFs is 6.1 while a significantly lower Pt-Pt coordination number of 2.7 was found in the Pt/f-CNFs. With the assumption of spherical particles,⁹ the average particle size is estimated to be about 1 nm and less than 0.6 nm for the Pt/p-CNFs and Pt/f-CNFs, respectively.

Very small metal clusters of about 0.5 nm in diameter was also reported in the literature for Pd supported on a platelet-type CNF with a graphite interplanar spacing of 0.340 nm.³⁵ These particle sizes are also smaller than those obtained by TEM as well as the electrochemical CV method. It has been previously demonstrated that the average metal particle size determined from the EXAFS coordination number is more accurate than TEM results if the average metal particle size is smaller than 2 nm,³⁶ which is due to the limited resolution of TEM under specified circumstances.

Table 3. Mean Pt-Pt coordination number and interatomic distance of reduced catalysts from EXAFS analysis and MD simulations

Sample	Scatter	Experimental			Simulated			
		Coordination Number	Interatomic distance [nm]	$2s^2 [\text{\AA}^2]^a$	Coordination number		Interatomic distance [nm]	
Pt/p-CNF	first-shell Pt-Pt	6.1	0.276	0.012	6.15 ^b	6.12 ^c	0.287 ^b	0.288 ^c
	second-shell Pt-Pt	3.0	0.392	0.018	2.53 ^b	2.73 ^c	0.377 ^b	0.374 ^c
Pt/f-CNF	first-shell Pt-Pt	2.7	0.271	0.013	2.64 ^d		0.293 ^d	
	second-shell Pt-Pt	0.6	0.387	0.013	1.64 ^d		0.379 ^d	

^a Debye-Waller type factor

^b Obtained from Pt atoms involved in Pt₅₀ clusters adsorbed at armchair site of p-CNFs

^c Obtained from Pt atoms involved in Pt₅₀ clusters adsorbed at zigzag arrangements of p-CNFs

^d Obtained from Pt atoms involved in six Pt₁₃ clusters adsorbed on f-CNFs

Although EXAFS provides some structural parameters of the fine structure of the supported Pt particles, a more detailed picture of how the Pt nanoparticles are reconstructed upon deposition has not yet been achieved. MD simulations based on the ReaxFF reactive force field, in combination with the EXAFS results, were therefore performed to demonstrate the structural

evolution of Pt nanoparticles adsorbed on both the p-CNFs and f-CNFs. As mentioned above, the Pt particle sizes estimated by the EXAFS analysis are 1 nm and less than 0.6 nm on the p-CNFs and f-CNFs, respectively. Hence, two Pt nanoparticles with approximately the same cluster sizes, namely, Pt_{50} and Pt_{13} , were constructed and deposited on the respective CNF models. Upon 150 ps of equilibrium, the size of the Pt clusters are measured to be 1.10 nm and 1.12 nm for the Pt_{50} at the armchair and zigzag arrangements of the p-CNFs, and 0.55 nm for the Pt_{13} on the f-CNFs, which indicates that these two metal-support combinations are well suited to the representation of the experimentally observed morphologies of CNF-supported Pt clusters.

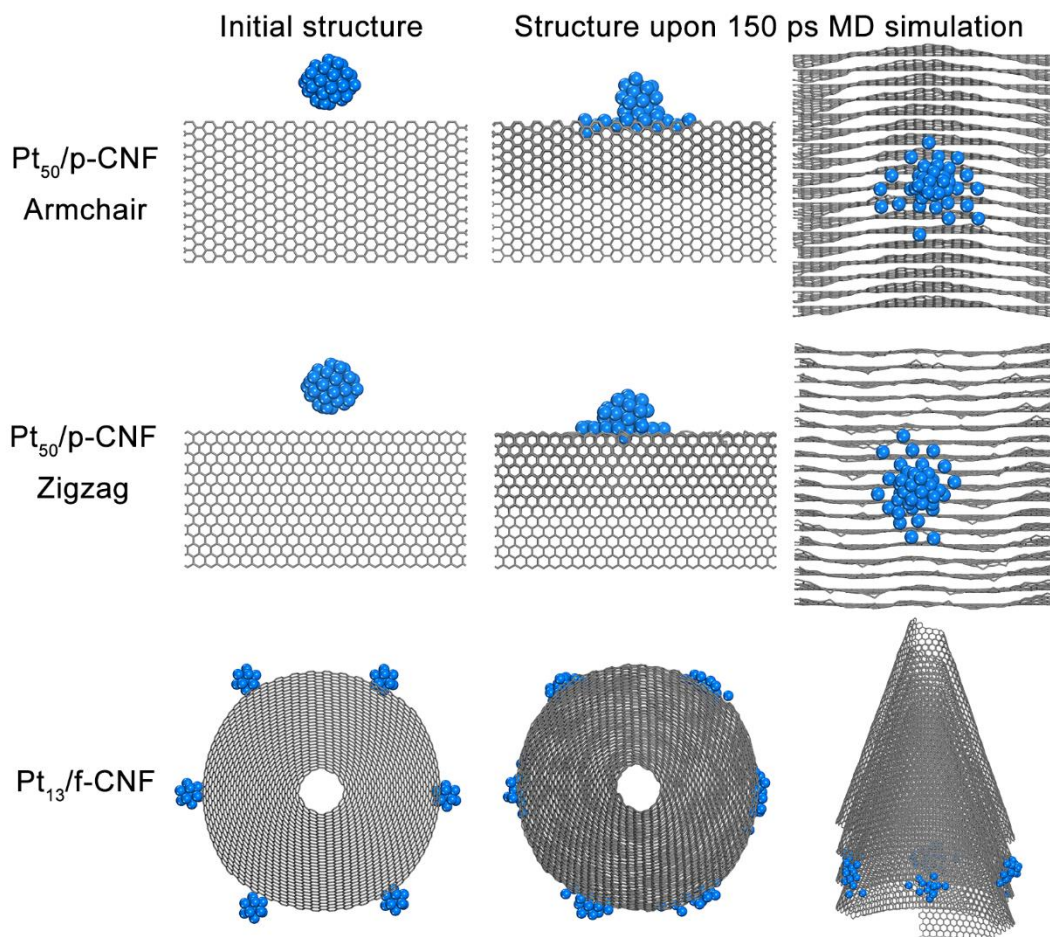


Figure 5. Schematic representations of Pt_{50} clusters adsorbed at the armchair and zigzag arrangements of p-CNFs and Pt_{13} clusters adsorbed on f-CNFs

The evolution of the Pt₅₀ and Pt₁₃ clusters upon adsorption is schematically represented in Figure 5. The comparison between the initial and relaxed structure upon 150 ps of equilibrium indicates that a fraction of Pt atoms are detached from the Pt clusters and then bonded to the CNF surfaces, which is ascribed to the strong metal-support interactions. Furthermore, it can be seen from the figure that the Pt clusters supported on the f-CNFs experience far more significant restructuring than the p-CNF supported Pt particles, and tend to ‘wet’ (spread over) the support surfaces with a contact angle close to 0 °. Meanwhile, a highly disordered structure is adopted by the nanometer-sized Pt assemblies on the f-CNFs, which is consistent with the TEM observations shown in Figure 2c and 2d.

To make a direct comparison between the microstructures of the supported Pt nanoparticles by theoretical predications and experimental EXAFS data, the mean Pt-Pt coordination number and interatomic distance of Pt atoms involved in the clusters were calculated, as presented in Table 3, where the first- and second-shell coordination numbers are derived from the data at the short (from 0.24 to 0.32 nm) and long (from 0.32 to 0.43 nm) Pt-Pt interatomic distances, respectively.

For the Pt₅₀ cluster adsorbed at the armchair configuration of the p-CNFs, the mean first- and second-shell Pt-Pt coordination numbers are calculated to be 6.15 and 2.53, respectively, and at the zigzag configuration the corresponding data are 6.12 and 2.73, respectively, which indicates that the arrangement of carbon atoms on the exposed CNF surfaces has a negligible effect on the bulk structure of supported Pt nanoparticles. Given the mean first-shell Pt-Pt coordination number of 8.15 in isolated Pt₅₀ clusters,³⁰ it can be deduced that the Pt clusters undergo severe but similar degree of reconstruction upon adsorption in the two configurations.

The calculated Pt-Pt coordination numbers and interatomic distances in both the Pt₅₀/p-CNF and the Pt₁₃/f-CNF are in line with the EXAFS results. In particular, the prediction of the first-

shell Pt-Pt coordination number gives almost the same values as the experimental measurements (6.1 and 2.7 for the Pt₅₀/p-CNF and Pt₁₃/f-CNF, respectively). This demonstrates that MD simulations with the usage of proper metal-carbon ReaxFF forcefield parameters are a powerful technique for analyzing the microstructures of carbon-supported metal nanoparticles at an atomic level.

3.4. Fine structures of the interface between Pt nanoparticles and CNF supports

A previous XANES and EXAFS study of a similar system indicated that it is normally not possible to differentiate between the contribution from Pt-O and Pt-C backscatters,¹¹ and therefore both the Pt-O and the Pt-C coordination are regarded as Pt coordinated to the CNF surface in the present work. In Table 4, the Pt-O and/or Pt-C coordination numbers at short and long interatomic distances are given for the Pt/p-CNF and Pt/f-CNF samples. The short interatomic distance is measured to be 0.211 and 0.218 nm for the Pt/p-CNFs and Pt/f-CNFs, respectively, which is close to 0.209 nm, the sum of the atomic radii of Pt (0.138 nm) and C (0.071 nm), and the long Pt-C interatomic distance (0.270 and 0.264 nm) has elsewhere been ascribed to the presence of interfacial hydrogen and to the interaction between Pt clusters and the CNF basal planes.^{11, 16} It can be seen from Table 4 that the experimentally predicted overall Pt-C coordination numbers (with both the short and the long Pt-C interatomic distances taken into account) in the Pt/p-CNFs and Pt/f-CNFs are 2.1 and 6.0, respectively, which are rather close to the MD results. Furthermore, the short and long Pt-C interatomic distances are also well represented by MD simulations. On the other hand, both experimental and calculated data indicate that the overall Pt-C coordination number in the Pt/p-CNFs differs significantly from that in the Pt/f-CNFs, which can be explained by the significant difference in morphologies of the Pt clusters supported on CNFs (as shown in Figure 5).

Table 4. Mean Pt-C coordination number from EXAFS analysis and MD simulations

Sample	Scatter	Experimental			Simulated			
		Coordination number	Interatomic distance [nm]	$2s^2$ [\AA^2] ^a	Coordination number	Interatomic distance [nm]		
Pt/p-CNF	overall Pt	0.9	0.211	0.007	1.04 ^b	1.28 ^c	0.204 ^b	0.206 ^c
	second-shell Pt-C	1.2	0.270	0.010	2.37 ^b	1.57 ^c	0.244 ^b	0.236 ^c
	interfacial Pt	~1.6			1.91 ^b	2.46 ^c		
	second-shell Pt-C	~2.2			4.37 ^b	3.03 ^c		
Pt/f-CNF	overall Pt	2.2	0.218	0.013	0.68 ^d		0.201	
	second-shell Pt-C	3.8	0.264	0.004	4.91 ^d		0.249	
	interfacial Pt	~2.2			0.77 ^d			
	second-shell Pt-C	~3.8			5.58 ^d			

^a Debye-Waller type factor

^b Obtained from Pt₅₀ clusters adsorbed at the armchair arrangements of p-CNFs

^c Obtained from Pt₅₀ clusters adsorbed at the zigzag arrangements of p-CNFs

^d Obtained from Pt₁₃ clusters adsorbed on f-CNFs

With the assumption of Pt nanoparticles as a half-spherical particle adopting an FCC crystal structure, the fraction of Pt atoms at the Pt-CNF interface was calculated by $f = 4R/d$, where R is the atomic radius of Pt and d is the Pt particle size.¹¹ By applying R = 0.138 nm, d = 1.0 nm, and an overall Pt-C coordination number of 0.9, an interfacial coordination number of 1.6 was obtained for the first-shell Pt-C coordination in the Pt/p-CNFs. Here the interfacial Pt-C coordination number is defined as the total number of Pt-C coordination at the metal-support interface divided by the total number of interfacial Pt atoms. As for the Pt/f-CNFs, however, the resultant interfacial coordination numbers are almost identical to the measured overall

coordination numbers. Given that the Pt particles that are smaller than 0.6 nm introduces uncertainty about the cluster geometry,³⁷ it is hard to get the exact value for the number of interfacial Pt atoms in the Pt/f-CNFs. Nevertheless, the interfacial Pt-C coordination numbers would be very close to the overall coordination numbers because in the small (< 0.6 nm) and highly dispersed Pt particles deposited on f-CNFs,¹¹ the majority of the Pt atoms in the Pt nanoparticles are located at the Pt-CNF interface. This has been verified by MD simulations, which indicate that for the Pt atoms at the Pt₁₃-f-CNF interface the calculated Pt-C coordination number (6.35 with both short and long Pt-C interatomic distances considered) is comparable to the calculated overall Pt-C coordination number (5.59), as given in Table 4.

It should be noted that our EXAFS analysis gives different Pt-C coordination numbers for the Pt/f-CNFs from the one reported in the literature where an f-CNF-supported Pt catalyst was prepared by deposition-precipitation and fourfold Pt-C coordination was attributed to the Pt nanoparticles being supported by adjacent graphene sheets.¹¹ In order to depict the Pt-CNF interface in a more detailed way, we examined the adsorption configurations of Pt atoms on the p-CNFs and f-CNFs, which are classified into four categories and shown schematically in Figure 6. First, Pt atoms are preferentially bonded to the edge planes of graphene sheets because basically accommodating a Pt atom on the edge planes are energetically more favorable than that on the basal planes.¹⁶ In Figure 6a, one can see that the first-shell Pt-C coordination number (at the short Pt-C interatomic distance) keeps to be 2, regardless of the arrangement of edge planes. However, the second shell Pt-C coordination number (at the longer Pt-C interatomic distance) depends strongly on the edge arrangement. At the armchair arrangement, the second shell Pt-C coordination number could take the value of 2 or 0, while at the zigzag arrangement the second shell Pt-C coordination number is 1. Second, as the Pt cluster size is larger than the CNF

interplanar spacing, it is possible for Pt atoms to interact with two adjacent graphite layers of CNFs. The difference in exposed CNF surface structures would give rise to a variation in Pt-C coordination number. For example, Pt atoms interact more probably with basal planes as the CNF apex angle is decreased, thereby leading to a higher possibility of formation of long Pt-C bonds and an increase in Pt-C coordination number. Therefore, the difference in the f-CNF morphology is probably responsible for the aforementioned discrepancy between our measured Pt-C coordination number and the data in the literature. As another example, the f-CNFs have a higher basal-to-edge surface area ratio than the p-CNFs and, consequently, long Pt-C bonds are preferred in the Pt/f-CNFs (see Figure 6b and 6c for comparison). Moreover, since the interfacial Pt atoms can simultaneously be bonded to the edge and basal planes of the f-CNFs, stronger metal-support interactions (and hence a higher restructuring degrees of the metal clusters) are expected on the Pt/f-CNFs. Finally, if Pt atoms are adsorbed on the f-CNF basal planes and positioned at a distance far away from the edge planes (see Figure 6d), the formation of long Pt-C covalent bonds would be promoted even more dramatically. Here the illustrations of Pt atoms bonded to the p-CNFs and f-CNFs are based on the ideal crystalline structures of the armchair and zigzag configurations. Under realistic experimental conditions, the surface of CNFs are far more complex and have surface defects such as sp^3 -hybridized and/or disordered carbon and/or dangling bonds. Nevertheless, the configuration information above clearly indicates that the surface structure of CNF supports plays a key role in determining the Pt-C coordination at the interface, which in turn has a significant effect on the interaction between Pt clusters and CNF supports.

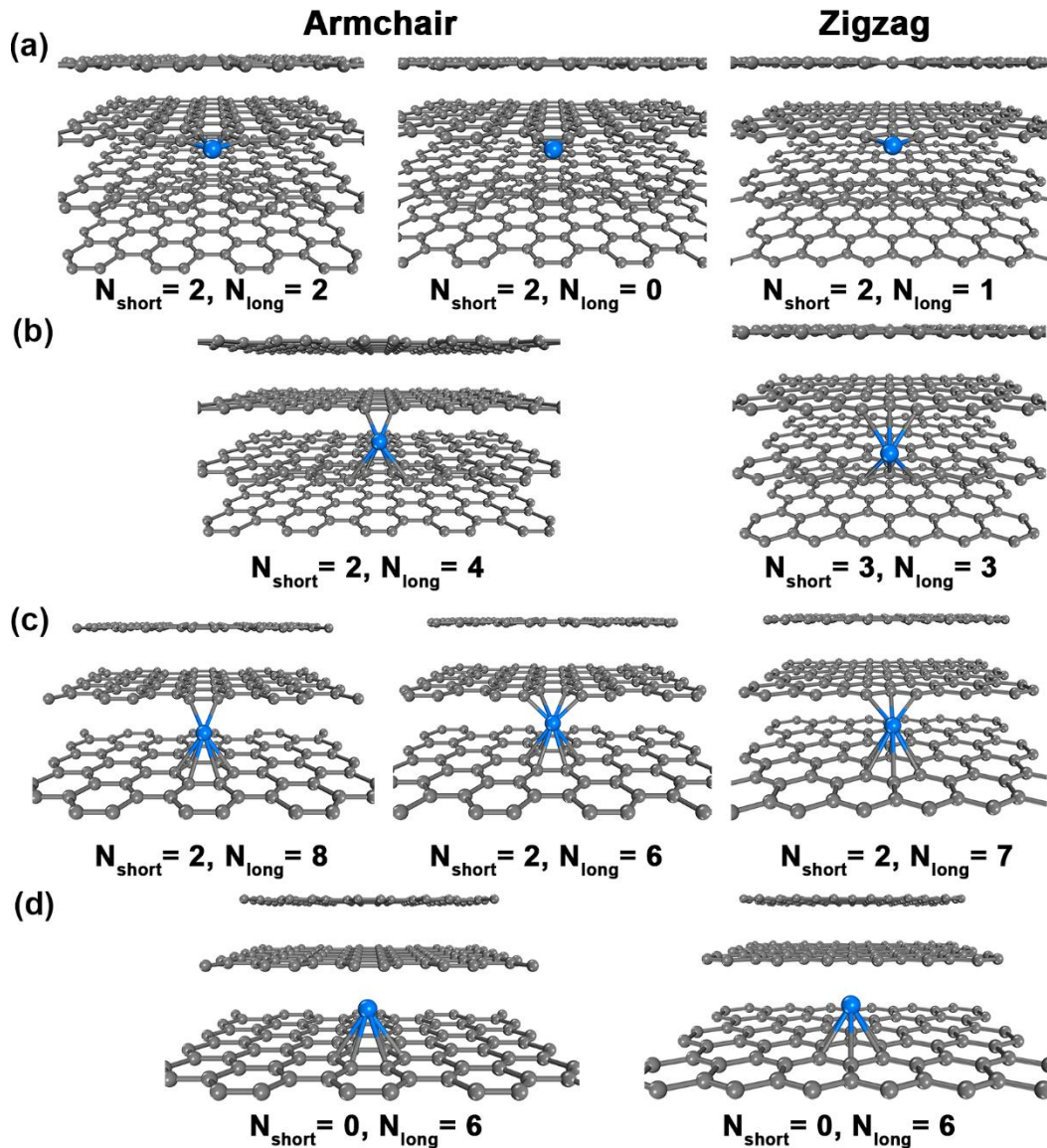


Figure 6. Schematic representations of Pt atoms bonded to p-CNFs and f-CNFs. (a) A Pt atom bonded to the edge planes of p-CNFs and f-CNFs; (b) A Pt atom bonded to two adjacent edge planes of p-CNFs; (c) A Pt atom bonded simultaneously to the basal and edge planes of f-CNFs; (d) A Pt atom bonded to the f-CNF basal planes. The numbers of short (from 0.18 nm to 0.22 nm) and long (from 0.22 nm to 0.28 nm) Pt-C bonds are denoted as N_{short} and N_{long} , respectively.

At the interface between the Pt clusters and p-CNFs, the Pt-C coordination numbers are experimentally estimated to be about 1.6 and 2.2, and the interatomic distances 0.211 and 0.270

nm for the first-shell and second-shell, respectively. The MD simulation results depends strongly on the graphene sheet termination such as “zigzag” or “armchair” arrangement. The simulated interatomic distances for the armchair termination of 0.204 and 0.244 nm at the first-shell and second-shell, respectively, are closer to the experimentally estimated values of 0.211 and 0.270 nm than those for the zigzag termination. In addition, the MD simulations predicts that the first-shell Pt-C coordination number of 1.91 at the interface for the armchair termination compares more closely to the experimental value of 1.6. It is therefore likely that the armchair arrangement dominates the graphene sheet termination in the p-CNF-supported Pt catalysts.

3.5. CO preferential oxidation on Pt/CNFs

To elucidate the effect of the structures of metal-support interfaces (and hence the structures of metal nanoparticles) on their adsorption and catalytic properties, CO preferential oxidation in a hydrogen-rich environment was then studied on the CNF-supported Pt catalysts at different temperatures. The conversions of CO and hydrogen oxidation are presented in Figure 7a and 7b, respectively. One can see that CO oxidation occurs at much lower temperatures than does hydrogen oxidation, which suggests that CO can be preferentially oxidized over hydrogen on the CNF-supported Pt catalysts. Although this oxidation activity is slightly lower than that of the CeO₂-supported Pt catalysts,³⁸⁻³⁹ it seems to be much higher than that of the γ -Al₂O₃-supported Pt catalysts,³⁹⁻⁴² where noticeable PROX activities were observed only at above 150°C. More interestingly, it is observed that the rate of CO oxidation depends significantly on the structure of the CNFs used as the supports. For instance, the temperature achieving 37 % conversion of CO is 77°C on the Pt/p-CNF, which is much lower than that on the Pt/f-CNF (124°C). As another example, the CO conversions at 77°C are 37 % and 11 % on the Pt/p-CNF and Pt/f-CNF,

respectively; that is, the rate of CO oxidation is more than 2 times higher on the Pt nanoparticles supported on the p-CNF than on the f-CNF.

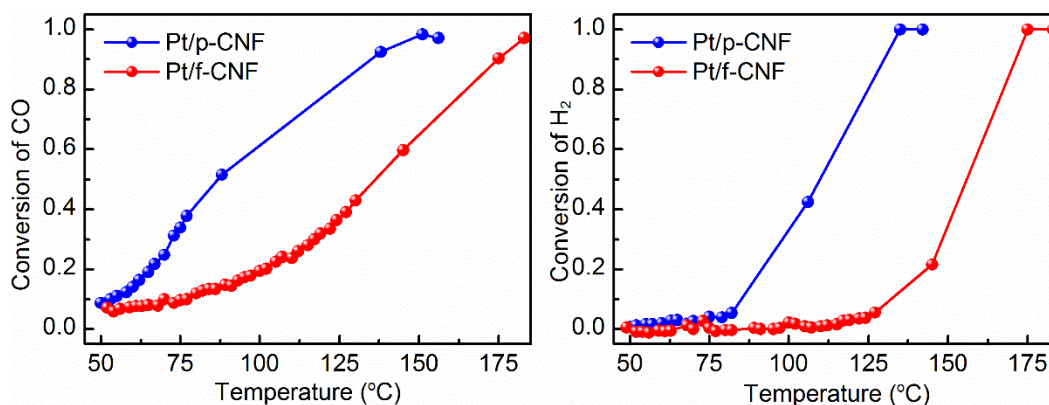


Figure 7. Preferential oxidation of CO in a mixture of CO and H₂. The ratio of CO/H₂/O₂/He is 0.01/1/0.5/100, and the total flow rate is 812 ml/min on the Pt/p-CNFs and Pt/f-CNFs.

On the other hand, the oxidation of hydrogen shows completely different character compared to the CO oxidation reaction. At low temperatures, hydrogen oxidation occurs very slowly. Once it ignites at certain temperatures, however, the rate for the hydrogen oxidation reaction increases abruptly with temperature. The ignition temperature of 77°C on the Pt/p-CNFs is much lower than that on the Pt/f-CNFs (120°C). Thus, the selective oxidation of CO is achieved at low temperatures, and the selectivity toward CO oxidation is over 90 % before the ignition of hydrogen oxidation.

The observed catalytic performance of the CNF-supported Pt catalysts for the selective oxidation of CO differs dramatically from that of the Pt nanoparticles supported on CeO₂,³⁸⁻³⁹ γ -Al₂O₃,⁴¹ and zeolites⁴³. It has been reported that on the Pt/ γ -Al₂O₃ the maximum selectivity toward CO oxidation is typically about 50 %, ⁴⁰⁻⁴² and 60 % in the presence of water.⁴² Although the dispersion of Pt varies significantly from 100 % to 60 %, ⁴¹ or from 8.9 % to 5.6 % ⁴² on γ -Al₂O₃, the selectivity is quite close, which suggests that the selectivity toward CO conversion is

insensitive to the Pt particle size. On the CeO₂-supported Pt catalysts, the selectivity of 100 % was reported at 50 % conversion on 3 nm Pt nanoparticles,³⁹ but relatively low selectivity was also observed on the Pt nanoparticles of 1.6 nm and 5.6 nm (< 40 %).³⁸ As for the Pt catalysts supported on zeolites, a higher selectivity was obtained than that on γ -Al₂O₃, and the selectivity decreases in the order Pt/A > Pt/mordenite > Pt/X > Pt/ γ -Al₂O₃.⁴³ The experimental findings in this work, together with the results in the literature, imply a strong support dependence of the selectivity in preferential oxidation of CO.

The oxidation of CO and H₂ typically involves adsorption/desorption processes and Langmuir surface reactions. The adsorption heat of CO [~ 140 kJ/mol on Pt(111)]⁴⁴⁻⁴⁶ is much higher than that of hydrogen [~ 80 kJ/mol on Pt(111)].⁴⁷ It results in a preferential adsorption of CO on Pt compared to hydrogen, which helps explain the experimentally observed preferential oxidation of CO and suppressed H₂ oxidation at low temperatures. Furthermore, the difference in the ignition temperatures of H₂ on the two different catalysts could reflect the difference in their ability to bind CO. The much higher ignition temperature of H₂ oxidation on the Pt/f-CNFs than that on the Pt/p-CNFs is indicative of a stronger binding of CO to the former.

To examine the adsorption behavior of CO on the CNF-supported Pt clusters in a more detailed way, kinetic modeling and analysis were performed for the preferential oxidation of CO. At very low reactant pressures, the rate for the oxidation of CO can be expressed in terms of the partial pressures of CO (P_{CO}) and O₂ (P_{O_2}):⁴⁸⁻⁴⁹

$$r_{CO} = k \cdot P_{CO} P_{O_2}^{0.5} \quad (1)$$

If O₂ is in large excess, then to a good approximation its partial pressure is constant throughout the reaction. We can therefore approximate P_{O_2} by $P_{O_2,0}$ and write

$$r_{CO} = k' \cdot P_{CO} \quad \text{and} \quad k' = k \cdot P_{O_2,0}^{0.5} \quad (2)$$

which has the form of the first-order rate law where k' is a lumped rate constant [mol / (g Pt·s·bar)]. If the reaction is thought of as occurring in an ideal isothermal plug flow reactor, which is a reasonable simplification for a typical fixed-bed reactor, the reactor design equation can be written as

$$\frac{dX}{dW / F_{CO,0}} = k' \cdot P_{CO,0} \cdot (1 - X) \quad (3)$$

where X is the CO conversion, W is the Pt weight [g], $F_{CO,0}$ is the CO molar flow rate [mol/s], and $P_{CO,0}$ is the initial partial pressure of CO [bar]. On integration of Eq. (1), the reaction rate at zero (inlet) conversion, r_{CO} , can be defined as

$$r_0 = k' \cdot P_{CO,0} = \frac{-\ln(1 - X) \cdot F_{CO,0}}{W} \quad \left(\frac{\text{mol}}{\text{gPt} \cdot \text{s}} \right) \quad (4)$$

Under this definition, the corresponding TOF values obtained at different temperatures were plotted against temperature, as shown in Figure 8. From the least squares fitted lines, one can see that the activation energies for CO preferential oxidation are 56.8 and 25.4 kJ/mol for the Pt/p-CNF and Pt/f-CNF, respectively, which fall well within the previously reported CO oxidation barriers ranging widely from 27 kJ/mol on the Pt/fiberglass⁵⁰ to 50.2 - 56.1 kJ/mol on the Pt/SiO₂,^{48, 50} and even to 137 kJ/mol on the single crystal Pt(100) surface.⁴⁸ Meanwhile, the pre-exponential factors of 1.38×10^{10} and 7.44×10^4 are given by the intercepts of the straight lines, and based on the transition state theory the apparent entropies of activation are estimated to be -154.6 and -53.7 J/mol·K for the Pt/f-CNFs and Pt/p-CNFs, respectively, which provides a

measure of the entropy change from the gaseous reactants of CO and O₂ to the rate-determining transition state. Although one cannot separate the individual entropy change of CO from that of O₂, the resultant larger magnitude of the entropy change on the Pt/f-CNFs implies lower mobility of the transition state than that on the Pt/p-CNFs. Since it is generally agreed that the transition state resembles the adsorption configuration of reactive intermediates, it is reasonable to expect that the reactants are bound more strongly to the Pt/f-CNFs than to the Pt/p-CNFs.

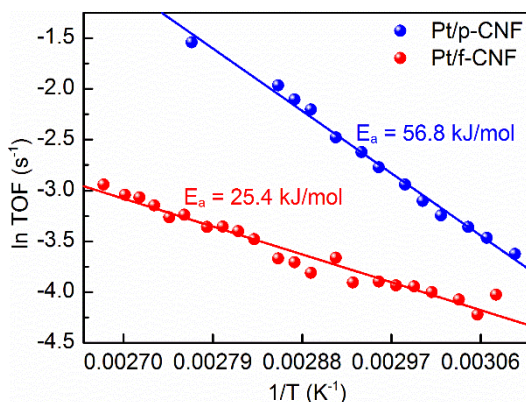


Figure 8. The Arrhenius plot of CO preferential oxidation under the conditions identical to the ones in Figure 7.

3.6. General discussion

As mentioned above, the Pt clusters deposited on the two CNFs with different graphene sheet orientations exhibit remarkably different catalytic activity for preferential oxidation of CO in a mixture of CO and H₂. The catalytic activity of the Pt/p-CNFs is much higher than that of the Pt/f-CNFs. The effects of the CNF support on the structural, adsorption, and catalytic properties of the Pt nanoparticles can be explained as follows.

First, the dispersion of the Pt clusters is directly influenced by the surface structures of the CNF supports. Combined EXAFS and MD results indicate that the CNF-supported Pt catalysts

can be finely dispersed on the two supports and have dimensions in the sub-nanometer regime. Moreover, the different CNF surface structures give rise to different Pt-CNF interfaces, and smaller Pt clusters with much rougher surfaces are found to be deposited on the f-CNFs. By analyzing the chemical bonding between the Pt and CNFs at their interfaces, it is suggested that the unique surface structure of the f-CNF leads to a much stronger Pt-CNF interaction and, consequently, to a higher Pt dispersion, which provides a rational interpretation of the lower Pt-Pt coordination numbers observed on the Pt/f-CNF. It should be noted that on the sub-nanometer scale, both the conventional TEM and CV measurements fail to provide us with valuable information about the Pt particle size, and even worse, they could make a wrong prediction about the relative sizes, as is the case for the Pt/p-CNFs and Pt/f-CNFs by using TEM.

Second, the geometrical structures (and hence the adsorption properties) of Pt active sites depend strongly on the metal-support interaction. As aforementioned, the strong Pt-f-CNF interaction leads to a decrease in particle size, which in turn increases the fraction of under-coordinated atoms on the metal surfaces. According to the *d*-band model,⁵¹⁻⁵² transition metal atoms with a low coordination number tend to have high-lying *d*-bands and thus bind the adsorbates more strongly than those on close-packed surfaces. On the other hand, a significant reconstructing of Pt particles upon deposition has previously been reported when the particle size is below 2 nm,³⁰ where the computed Pt-Pt first-shell coordination number and Pt-Pt bond length on the exposed surfaces are found to decrease and increase, respectively. The increased Pt-Pt bond length would also shift the *d*-band center toward a higher value, thereby enhancing the binding of adsorbates to the metal surface.

The structure sensitivity of CO oxidation on transition metal catalysts has long been observed and makes it a good prototype reaction of rational catalysis science. It is generally accepted that

the recombination of adsorbed CO and O is the rate-determining step for this reaction,⁵³⁻⁵⁵ and therefore the overall reaction rate depends strongly on the surface coverages of CO and O. Under some experimental conditions such as low reaction temperature and high CO partial pressures, the surface is predominantly covered by CO and, consequently, the reaction rate is affected by the probability that CO desorbs to release surface sites for oxygen dissociation. For example, Zafiris and Gorte suggested that 14 nm Pt catalysts give a 10 times greater TOF for CO oxidation than those with a particle size of 1.7 nm because CO is less strongly bound to planar facets that dominate large Pt particles.⁵⁶ Santra et al. believed that CO adsorbed on the close-packed surfaces is more active than that at the step sites, and oxygen atoms chemisorbed at the step sites are more facile in interacting with CO adsorbed on the terraces.⁵⁵ It was later demonstrated by Atalik and Uner that the TOF for the CO oxidation reaction changes with the desorption kinetics of CO, and the increase in the TOF with Pt particle size is accompanied by a decrease in the apparent activation energy.⁵⁷ In the present work, however, both the TOF for CO oxidation and the apparent activation energy are found to be lower on the smaller f-CNF-supported Pt clusters. The origin of this discrepancy may probably lies in the fact that the pre-exponential factor is dependent strongly on the local geometry of active sites as well as the binding strength of CO. On the smaller f-CNF-supported Pt nanoparticles, the more abundant coordinately unsaturated surface sites and higher restructuring degree result in a significantly stronger CO adsorption, so that the decrease in the pre-exponential factor activation energy cannot be compensated for by the decrease in the apparent activation energy, thus leading to a lower reaction rate than that on the Pt/p-CNFs.

Third, the CNF supports can modify the electronic properties of the sub-nanometer Pt clusters.

In general, the electronic effect of the support is restricted to the region very close to the metal-

support interface. However, when the dimensions of metal nanoparticles are decreased to a very low level, in the sub-nanometer regime in the Pt/f-CNF case, the electronic structures of all component metal atoms might be affected by the presence of the support. Our XANES results seem to reveal that at reaction temperatures there exists an electron transfer from the Pt to CNFs, in good agreement with previous observations,⁵⁸⁻⁶⁰ and, more importantly, the smaller f-CNF-supported Pt clusters are found to be more positively charged than the Pt/p-CNF. It has been proposed that the positively charged Pt atoms may interact more strongly with CO because of their capability of accepting a larger amount of electron density from the CO 5 σ orbitals by σ -donation.⁶¹ Indeed, the higher ignition temperature of hydrogen oxidation on the Pt/f-CNF provides direct evidence in support of the enhanced CO adsorption arising from the stronger metal-support interactions.

The work here indicates that the CNF structure has a significant effect on the properties of the supported Pt clusters. It opens up new opportunities in catalyst design to use differently structured CNFs as a platform to tune the metal reactivity through manipulating the surface structures of CNFs and the metal-support interaction. For the preferential CO oxidation and hydrogen oxidation reactions,⁸ the p-CNF is an effective support which can provide stable but more smooth Pt surfaces to adsorb CO with a proper binding strength. In this regard, the Pt/p-CNFs could be a good catalyst for fuel cells, and its superior performance has elsewhere been reported.^{6, 62} On the other hand, the combined graphene edge and basal planes on the f-CNF surfaces would lead to a very strong interaction between Pt and CNFs, resulting in formation of sub-nanometer Pt clusters. For structure-insensitive reactions, smaller Pt particles can give higher dispersion and thus higher catalytic activity.

4. Conclusions

In this work, we have demonstrated XANES and EXAFS analysis combined with MD simulations as a powerful technique for studying the interaction of Pt clusters with CNFs. It provides detailed atomic-level insight and visualization of the fine structures of the Pt-CNF interfaces and supported Pt clusters. For the first time, the different catalytic behaviors of Pt clusters deposited on various CNF structures are rationalized. For the Pt atoms at the interface between the CNFs and Pt clusters, both EXAFS analysis and MD simulations indicate that the Pt-C coordination number depends strongly on the CNF surface structure, where Pt is preferably bonded to the edges of the graphene sheets in the p-CNFs while the stronger adsorption at both the edge and basal planes in the f-CNFs yields a much more significant restructuring of the Pt clusters. Neither the conventional TEM nor CV measurements can provide us with correct information about the Pt particle size. The Pt-Pt coordination number determined from EXAFS suggests that smaller Pt sub-nanoparticles (less than 0.6 nm in size) are supported on the f-CNFs than those on the p-CNFs (~ 1 nm in size). The higher Pt-Pt coordination number on the Pt/p-CNFs gives rise to a weaker adsorption of CO, and consequently, to a higher catalytic activity for the oxidation reactions, which helps explain why the Pt/p-CNF is a promising fuel cell catalyst. These experimental and theoretical findings give new opportunities for rational catalyst design using CNF as a platform to tailor the structural properties of Pt to a particular chemical reaction.

Acknowledgements

This work is supported by the Research Council of Norway, Natural Science Foundation of China (21406063, 21473053, and 91645122), and the Fundamental Research Funds for the Central Universities (222201718003). We acknowledge the staff at the Swiss-Norwegian Beam

Lines (SNBL) at ESRF for their assistance. The computational time provided by the Notur project is highly acknowledged.

References

1. Cheng, H. Y.; Zhu, Y. A.; Sui, Z. J.; Zhou, X. G.; Chen, D., Modeling of Fishbone-Type Carbon Nanofibers with Cone-Helix Structures. *Carbon* **2012**, *50* (12), 4359-4372.
2. Serp, P., Carbon Nanotubes and Nanofibers in Catalysis. In *Handbook of Heterogeneous Catalysis, Second, Completely Revised and Enlarged Edition*, Ertl, G.; Knözinger, H.; Schüth, F.; Weitkamp, J., Eds. Wiley: 2009; Vol. 1, pp 309-372.
3. Zhu, J.; Holmen, A.; Chen, D., Carbon Nanomaterials in Catalysis: Proton Affinity, Chemical and Electronic Properties, and their Catalytic Consequences. *Chemcatchem* **2013**, *5* (2), 378-401.
4. Tessonnier, J.-P.; Su, D. S., Recent Progress on the Growth Mechanism of Carbon Nanotubes: A Review. *Chemsuschem* **2011**, *4* (7), 824-847.
5. Truong-Huu, T.; Chizari, K.; Janowska, I.; Moldovan, M. S.; Ersen, O.; Nguyen, L. D.; Ledoux, M. J.; Pham-Huu, C.; Begin, D., Few-layer graphene supporting palladium nanoparticles with a fully accessible effective surface for liquid-phase hydrogenation reaction. *Catal. Today* **2012**, *189* (1), 77-82.
6. Muthuswamy, N.; de la Fuente, J. L. G.; Ochal, P.; Giri, R.; Raaen, S.; Sunde, S.; Ronning, M.; Chen, D., Towards a highly-efficient fuel-cell catalyst: optimization of Pt particle size, supports and surface-oxygen group concentration. *Phys. Chem. Chem. Phys.* **2013**, *15* (11), 3803-3813.
7. Li, P.; Huang, Y. L.; Chen, D.; Zhu, J.; Zhao, T. J.; Zhou, X. G., CNFs-supported Pt catalyst for hydrogen evolution from decalin. *Catal. Commun.* **2009**, *10* (6), 815-818.

8. Kvande, I.; Chen, D.; Zhao, T. J.; Skoe, I. M.; Walmsley, J. C.; Ronning, M., Hydrogen Oxidation Catalyzed by Pt Supported on Carbon Nanofibers with Different Graphite Sheet Orientations. *Top Catal* **2009**, *52* (6-7), 664-674.
9. de Graaf, J.; van Dillen, A. J.; de Jong, K. P.; Koningsberger, D. C., Preparation of highly dispersed Pt particles in zeolite Y with a narrow particle size distribution: Characterization by hydrogen chemisorption, TEM, EXAFS spectroscopy, and particle modeling. *J. Catal.* **2001**, *203* (2), 307-321.
10. Mojet, B. L.; Hoogenraad, M. S.; van Dillen, A. J.; Geus, J. W.; Koningsberger, D. C., Coordination of palladium on carbon fibrils as determined by XAFS spectroscopy. *J. Chem. Soc., Faraday Trans.* **1997**, *93* (24), 4371-4375.
11. Zhang, Y.; Toebes, M. L.; Van der Eerden, A.; O'Grady, W. E.; De Jong, K. P.; Koningsberger, D. C., Metal Particle Size and Structure of the Metal-Support Interface of Carbon-Supported Platinum Catalysts as Determined with EXAFS Spectroscopy. *J. Phys. Chem. B* **2004**, *108* (48), 18509-18519.
12. Billinge, S. J. L.; Levin, I., The Problem with Determining Atomic Structure at the Nanoscale. *Science* **2007**, *316* (5824), 561-565.
13. Sanz-Navarro, C. F.; Astrand, P. O.; Chen, D.; Ronning, M.; van Duin, A. C. T.; Mueller, J. E.; Goddard, W. A., Molecular dynamics simulations of carbon-supported Ni clusters using the Reax reactive force field. *J Phys Chem C* **2008**, *112* (33), 12663-12668.
14. Sanz-Navarro, C. F.; Astrand, P. O.; Chen, D.; Rønning, M.; van Duin, A. C. T.; Jacob, T.; Goddard, W. A., Molecular Dynamics Simulations of the Interactions between Platinum Clusters and Carbon Platelets. *J. Phys. Chem. A* **2008**, *112* (7), 1392-1402.

15. Sanz-Navarro, C. F.; Astrand, P. O.; Chen, D.; Ronning, M.; van Duin, A. C. T.; Goddard, W. A., Molecular Dynamics Simulations of Metal Clusters Supported on Fishbone Carbon Nanofibers. *J Phys Chem C* **2010**, *114* (8), 3522-3530.
16. Cheng, H. Y.; Zhu, Y. A.; Astrand, P. O.; Chen, D.; Li, P.; Zhou, X. G., Evolution of Pt Nanoparticles Supported on Fishbone-Type Carbon Nanofibers with Cone-Helix Structures: A Molecular Dynamics Study. *J. Phys. Chem. C* **2013**, *117* (27), 14261-14271.
17. Kvande, I.; Briskeby, S.; Tsyarkin, M.; Rønning, M.; Sunde, S.; Tunold, R.; Chen, D., On the preparation methods for carbon nanofiber-supported Pt catalysts. *Top. Catal.* **2007**, *45* (1), 81-85.
18. Toebe, M. L.; Bitter, J. H.; van Dillen, A. J.; de Jong, K. P., Impact of the structure and reactivity of nickel particles on the catalytic growth of carbon nanofibers. *Catal. Today* **2002**, *76* (1), 33-42.
19. Yu, Z.; Chen, D.; Totdal, B.; Holmen, A., Effect of Support and Reactant on the Yield and Structure of Carbon Growth by Chemical Vapor Deposition. *J. Phys. Chem. B* **2005**, *109* (13), 6096-6102.
20. Kvande, I.; Zhu, J.; Zhao, T. J.; Hammer, N.; Rønning, M.; Raaen, S.; Walmsley, J. C.; Chen, D., Importance of Oxygen-Free Edge and Defect Sites for the Immobilization of Colloidal Pt Oxide Particles with Implications for the Preparation of CNF-Supported Catalysts. *J. Phys. Chem. C* **2010**, *114* (4), 1752-1762.
21. Reetz, M. T.; Lopez, M. Method for in-situ immobilization of water-soluble nanodispersed metal oxide colloids. U.S. Patent 7,244,688 2003.
22. Reetz, M. T.; Koch, M. G., Water-Soluble Colloidal Adams Catalyst: Preparation and Use in Catalysis. *J. Am. Chem. Soc.* **1999**, *121* (34), 7933-7934.

23. Ressler, T. J., WinXAS : A New Software Package not only for the Analysis of Energy-Dispersive XAS Data. *J. Phys. IV France* **1997**, 7, C2-269-C2-270.
24. Shirley, E. L., Theory and simulation of resonant inelastic X-ray scattering in s-p bonded systems: graphite, hexagonal boron nitride, diamond, and cubic boron nitride. *J. Electron. Spectrosc. Relat. Phenom.* **2000**, 110 (1-3), 305-321.
25. Gurman, S. J.; Binsted, N.; Ross, I., A rapid, exact curved-wave theory for EXAFS calculations. *Journal of Physics C: Solid State Physics* **1984**, 17 (1), 143-51.
26. Guo, J. W.; Zhao, T. S.; Prabhuram, J.; Wong, C. W., Preparation and the physical/electrochemical properties of a Pt/C nanocatalyst stabilized by citric acid for polymer electrolyte fuel cells. *Electrochim. Acta* **2005**, 50 (10), 1973-1983.
27. LAMMPS WWW Site. <http://lammmps.sandia.gov>.
28. Plimpton, S., Fast Parallel Algorithms for Short-Range Molecular Dynamics. *J. Comput. Phys.* **1995**, 117 (1), 1-19.
29. Rappe, A. K.; Goddard, W. A., Charge Equilibration for Molecular-Dynamics Simulations. *J. Phys. Chem.* **1991**, 95 (8), 3358-3363.
30. Cheng, H. Y.; Zhu, Y. A.; Chen, D.; Astrand, P. O.; Li, P.; Qi, Z. W.; Zhou, X. G., Evolution of Carbon Nanofiber-Supported Pt Nanoparticles of Different Particle Sizes: A Molecular Dynamics Study. *J. Phys. Chem. C* **2014**, 118 (41), 23711-23722.
31. Martyna, G. J.; Klein, M. L.; Tuckerman, M., Nose-Hoover Chains: The Canonical Ensemble Via Continuous Dynamics. *J. Chem. Phys.* **1992**, 97 (4), 2635-2643.
32. Lukaszewski, M.; Soszko, M.; Czerwinski, A., Electrochemical Methods of Real Surface Area Determination of Noble Metal Electrodes - an Overview. *Int J Electrochem Sc* **2016**, 11 (6), 4442-4469.

33. Liu, C.; Bolin, T.; Northrup, P.; Lee, S.; McEnally, C.; Kelleher, P.; Pfefferle, L.; Haller, G. L., Combined Zr and S XANES Analysis on S-ZrO₂/MWCNT Solid Acid Catalyst. *Top. Catal.* **2014**, *57* (6), 693-705.
34. Reetz, M. T.; Lopez, M.; Gruenert, W.; Vogel, W.; Mahlendorf, F., Preparation of colloidal nanoparticles of mixed metal oxides containing platinum, ruthenium, osmium, and iridium and their use as electrocatalysts. *J. Phys. Chem. B* **2003**, *107* (30), 7414-7419.
35. Chesnokov, V. V.; Prosvirin, I. P.; Zaitseva, N. A.; Zaikovskii, V. I.; Molchanov, V. V., Effect of the Structure of Carbon Nanofibers on the State of an Active Component and on the Catalytic Properties of Pd/C Catalysts in the Selective Hydrogenation of 1,3-Butadiene. *Kinet. Catal.* **2002**, *43* (6), 838-846.
36. de Graaf, J., Metal-support interaction and sulfur tolerance of platinum/zeolite Y catalysts. Ph.D. Thesis, Utrecht University, Utrecht, The Netherlands. **2001**.
37. Nie, A. H.; Wu, J. P.; Zhou, C. G.; Yao, S. J.; Forrey, R. C.; Cheng, H. S., Structural evolution of subnano platinum clusters. *Int. J. Quantum Chem* **2007**, *107* (1), 219-224.
38. Pozdnyakova, O.; Teschner, D.; Wootsch, A.; Kröhnert, J.; Steinhauer, B.; Sauer, H.; Toth, L.; Jentoft, F. C.; Knop-Gericke, A.; Paál, Z.; Schlögl, R., Preferential CO oxidation in hydrogen (PROX) on ceria-supported catalysts, part I: Oxidation state and surface species on Pt/CeO₂ under reaction conditions. *J. Catal.* **2006**, *237* (1), 1-16.
39. Liu, Y. X.; Liu, B. C.; Liu, Y.; Wang, Q.; Hu, W. T.; Jing, P.; Liu, L. X.; Yu, S. L.; Zhang, J., Improvement of catalytic performance of preferential oxidation of CO in H₂-rich gases on three-dimensionally ordered macro- and meso-porous Pt-Au/CeO₂ catalysts. *Appl Catal B-Environ* **2013**, *142*, 615-625.

40. Avgouropoulos, G.; Ioannides, T.; Papadopoulou, C.; Batista, J.; Hocevar, S.; Matralis, H. K., A comparative study of Pt/ γ -Al₂O₃, Au/ α -Fe₂O₃ and CuO–CeO₂ catalysts for the selective oxidation of carbon monoxide in excess hydrogen. *Catal. Today* **2002**, 75 (1 – 4), 157-167.
41. Kim, D. H.; Lim, M. S., Kinetics of selective CO oxidation in hydrogen-rich mixtures on Pt/alumina catalysts. *Applied Catalysis A: General* **2002**, 224 (1–2), 27-38.
42. Manasilp, A.; Gulari, E., Selective CO oxidation over Pt/alumina catalysts for fuel cell applications. *Applied Catalysis B: Environmental* **2002**, 37 (1), 17-25.
43. Igarashi, H.; Uchida, H.; Suzuki, M.; Sasaki, Y.; Watanabe, M., Removal of carbon monoxide from hydrogen-rich fuels by selective oxidation over platinum catalyst supported on zeolite. *Applied Catalysis A: General* **1997**, 159 (1–2), 159-169.
44. Allian, A. D.; Takanabe, K.; Fujdala, K. L.; Hao, X.; Truex, T. J.; Cai, J.; Buda, C.; Neurock, M.; Iglesia, E., Chemisorption of CO and Mechanism of CO Oxidation on Supported Platinum Nanoclusters. *J. Am. Chem. Soc.* **2011**, 133 (12), 4498-4517.
45. Ertl, G.; Neumann, M.; Streit, K. M., Chemisorption of CO on the Pt(111) surface. *Surf. Sci.* **1977**, 64 (2), 393-410.
46. Steininger, H.; Lehwald, S.; Ibach, H., On the adsorption of CO on Pt(111). *Surf. Sci.* **1982**, 123 (2–3), 264-282.
47. Poelsema, B.; Mechttersheimer, G.; Comsa, G., The interaction of hydrogen with platinum(s)–9(111) \times (111) studied with helium beam diffraction. *Surf. Sci.* **1981**, 111 (3), 519-544.
48. Berlowitz, P. J.; Peden, C. H. F.; Goodman, D. W., Kinetics of carbon monoxide oxidation on single-crystal palladium, platinum, and iridium. *The Journal of Physical Chemistry* **1988**, 92 (18), 5213-5221.

49. Depcik, C.; Loya, S.; Srinivasan, A.; Wentworth, T.; Stagg-Williams, S., Adaptive Global Carbon Monoxide Kinetic Mechanism over Platinum/Alumina Catalysts. *Catalysts* **2013**, *3* (2), 517.
50. Cant, N. W.; Hicks, P. C.; Lennon, B. S., Steady-state oxidation of carbon monoxide over supported noble metals with particular reference to platinum. *J. Catal.* **1978**, *54* (3), 372-383.
51. Hammer, B.; Norskov, J. K., Why gold is the noblest of all the metals. *Nature* **1995**, *376* (6537), 238-240.
52. Ruban, A.; Hammer, B.; Stoltze, P.; Skriver, H. L.; Nørskov, J. K., Surface electronic structure and reactivity of transition and noble metals. *J. Mol. Catal. A-Chem* **1997**, *115* (3), 421-429.
53. Rashkeev, S. N.; Lupini, A. R.; Overbury, S. H.; Pennycook, S. J.; Pantelides, S. T., Role of the nanoscale in catalytic CO oxidation by supported Au and Pt nanostructures. *Phys. Rev. B* **2007**, *76* (3).
54. Wintterlin, J.; Völkening, S.; Janssens, T. V. W.; Zambelli, T.; Ertl, G., Atomic and Macroscopic Reaction Rates of a Surface-Catalyzed Reaction. *Science* **1997**, *278* (5345), 1931-1934.
55. Santra, A. K.; Goodman, D. W., Catalytic oxidation of CO by platinum group metals: from ultrahigh vacuum to elevated pressures. *Electrochim. Acta* **2002**, *47* (22-23), 3595-3609.
56. Zafiris, G. S.; Gorte, R. J., CO Oxidation on Pt/ α -Al₂O₃(0001): Evidence for Structure Sensitivity. *J. Catal.* **1993**, *140* (2), 418-423.
57. Atalik, B.; Uner, D., Structure sensitivity of selective CO oxidation over Pt/ γ -Al₂O₃. *J. Catal.* **2006**, *241* (2), 268-275.

58. Chen, W.; Duan, X.; Qian, G.; Chen, D.; Zhou, X., Carbon Nanotubes as Support in the Platinum-Catalyzed Hydrolytic Dehydrogenation of Ammonia Borane. *Chemsuschem* **2015**, *8* (17), 2927-2931.
59. Chen, W.; Ji, J.; Feng, X.; Duan, X.; Qian, G.; Li, P.; Zhou, X.; Chen, D.; Yuan, W., Mechanistic Insight into Size-Dependent Activity and Durability in Pt/CNT Catalyzed Hydrolytic Dehydrogenation of Ammonia Borane. *J. Am. Chem. Soc.* **2014**, *136* (48), 16736-16739.
60. Chen, W.; Ji, J.; Duan, X.; Qian, G.; Li, P.; Zhou, X.; Chen, D.; Yuan, W., Unique reactivity in Pt/CNT catalyzed hydrolytic dehydrogenation of ammonia borane. *Chem. Commun.* **2014**, *50* (17), 2142-2144.
61. Mahmoodinia, M.; Åstrand, P.-O.; Chen, D., Influence of Carbon Support on Electronic Structure and Catalytic Activity of Pt Catalysts: Binding to the CO Molecule. *The Journal of Physical Chemistry C* **2016**, *120* (23), 12452-12462.
62. Li, Z. Z.; Cui, X. L.; Zhang, X. S.; Wang, Q. F.; Shao, Y. Y.; Lin, Y. H., Pt/Carbon Nanofiber Nanocomposites as Electrocatalysts for Direct Methanol Fuel Cells: Prominent Effects of Carbon Nanofiber Nanostructures. *J Nanosci Nanotechno* **2009**, *9* (4), 2316-2323.

TOC

